Relaxor ferroeletric behavior in $Sr_{1-x}Pr_xTiO_3$: Cooperation between polar and antiferrodistortive instabilities

Stefano Checchia,[1] Mattia Allieta,[1,*] Mauro Coduri,[2,3] Michela Brunelli,[4] and Marco Scavini[1,5]
[1]*Dipartimento di Chimica, Università Degli Studi di Milano, via Golgi 19, 20133 Milano, Italy*
[2]*ESRF–The European Synchrotron, 71 Avenue des Martyrs, CS40220 38043 Grenoble, France*
[3]*CNR-ICMATE, Corso Promessi Sposi 29, Lecco, Italy*
[4]*SNBL–The Swiss-Norwegian Beamlines at the ESRF, 71 Avenue des Martyrs, CS40220 38043 Grenoble, France*
[5]*CNR-ISTM, Istituto Scienze e Tecnologie Molecolari, I-20133 Milan, Italy*
(Received 23 July 2016; revised manuscript received 8 August 2016; published 14 September 2016)

Chemical doping at the Sr and Ti sites is a feasible way to alter the quantum paraelectric state of $SrTiO_3$ perovskite. Doping with Pr is known to induce relaxor ferroelectricity at room temperature in the $Sr_{1-x}Pr_xTiO_3$ solid solution. The relationship between its dielectric properties and structural phase transition has been debated, but no definitive structural argument has been proposed. Here we present a systematic structural study of $Sr_{1-x}Pr_xTiO_3$ ($0.020 \leqslant x \leqslant 0.150$). We establish the structural phase diagram using high-resolution x-ray powder diffraction by finding the antiferrodistortive structural phase transitions for all the compositions studied. By using pair distribution function analysis, we show the mismatch between local and long-range structures in terms of increased local order parameters. Finally, we propose a correlation between the local structural order parameters and the emergence of hard polar modes as found by Raman spectroscopy. Our results are quantitatively consistent with recent theoretical calculations showing that the increase of local tetragonality and local octahedral tilting above a critical value in fact underlie the polar instability. This confirms that structural orders involving both polar and antiferrodistortive characters compete and cooperate at different levels, promoting ferroelectricity in $Sr_{1-x}Pr_xTiO_3$.

DOI: 10.1103/PhysRevB.94.104201

I. INTRODUCTION

Very few materials have attracted such tremendous interest as ferroelectric (FE) perovskites for both technological and scientific reasons [1–7]. These compounds have a spontaneous electric polarization that can be switched by applying an electric field, paving the way to design smart sensors, capacitors, and data storage devices [2]. Although a number of physical phenomena are known to produce FE response in perovskites [1], the microscopic nature of their mechanisms is often unclear.

Here we study the $Sr_xPr_{1-x}TiO_3$ solid solution, which has been widely reported to develop FE at room temperature [4–7]. Undoped $SrTiO_3$ has two soft modes: One is associated with an antiferrodistortive (AFD) phase transition from cubic $Pm\text{-}3m$ to tetragonal $I4/mcm$ [1], the other one with FE distortion [1]. Quantum fluctuations prevent condensation of the FE mode, giving $SrTiO_3$ a paraelectric phase down to 0 K [1]. It has been reported that perturbing this state by doping with the smaller Pr compared to Sr ($r_{Pr}/r_{Sr} \sim 0.9$) induces ferroelectricity in $Sr_xPr_{1-x}TiO_3$ at room temperature [4]. In particular, for low x values in $Sr_xPr_{1-x}TiO_3$ ($0.020 \leqslant x \leqslant 0.075$), Durán *et al.* detected a cubic structure at room temperature [4] accompanied by a dielectric permittivity anomaly at $T_m \sim 500$ K indicative of a *normal* ferroelectric-paraelectric transition [4]. The proposed FE picture seemed to be confirmed by their structural study showing evidence of Ti off-centering for $x = 0.150$ as a result of a $Pm\text{-}3m$ to $P4mm$ phase transition below $T_C = 391$ K [6].

This interpretation was rejected by Garg *et al.*, who pointed out that the difference between the T_m and T_C excluded a *normal* ferroelectric behavior [7]. Moreover, the same authors determined for $x > 0.05$ a centrosymmetric, AFD-distorted tetragonal phase (space group $I4/mcm$) by using both high-resolution synchrotron x-ray diffraction and neutron diffraction [7]. Having found that the tetragonal phase retained inversion symmetry, they argued that the appearance of the FE state in $Sr_{1-x}Pr_xTiO_3$ ($0.020 \leqslant x \leqslant 0.150$) well below the dielectric anomaly temperature could only be explained in terms of relaxor ferroelectricity [7].

The relaxor FE model implies that disorder produced by chemical doping at the A and B sites of the ABO_3 perovskite structure causes the formation of dipolar entities that coalesce into polar nanoregions (PNRs) even in structures that are centrosymmetric on average [3]. To allow this, a highly polarizable structure must host dopants that induce ordered FE domains, i.e., PNRs, embedded in a paraelectric phase. From the structural point of view, relaxor ferroelectricity in a $SrTiO_3$-like perovskite can be visualized in terms of fluctuations in the FE order parameter, i.e., atomic displacements on the A/B sites, and in the AFD order parameter, i.e., the tilting angle (ϕ) induced by doping [1–3]. Coexisting FE and AFD instabilities tend to compete and thus to cancel out [8], so that very small cation off-centerings ($\Delta \sim 0.01$ Å) are found in many Ti-based relaxor compounds [9,10]. This makes detecting the breaking of inversion symmetry in $Sr_xPr_{1-x}TiO_3$ a very complicated task, since the difference between the $4/mmm$ and $4mm$ point symmetries in the case of polar displacements of this magnitude is almost invisible to conventional crystallographic techniques.

Recently Aschauer and Spaldin [11] developed a new perspective on the interplay between $SrTiO_3$ structure and

*mattia.allieta@gmail.com

FE instability. By computing the energy gain due to FE as a function of ϕ, they found that the TiO_6 rotation indeed dampens the FE mode, but only for small ϕ angles. Larger ϕ angles ($>6^\circ$) combined with increased tetragonality do in fact enhance the FE distortion in order to recover the loss of Ti-O π bonding along the c axis [11]. Ultimately, their model implies that any structural relaxation affected by collective cation off-centerings can be related to increased tetragonality and tilting angle order parameters, an effect that, in our case, could be induced by doping. A similar picture was proposed to describe the origin of FE in strained $SrTiO_3$ epitaxial films [12] but it is not clear to date whether such a mechanism can be realized in the bulk structure.

In this paper, we have analyzed the structural response of relaxor ferroelectricity in $Sr_xPr_{1-x}TiO_3$ through a systematic x-ray powder diffraction study in a wide temperature and composition range ($0.020 \leqslant x \leqslant 0.150$). We confirmed the room-temperature tetragonal structure (s.g. $I4/mcm$) for every sample with $x \geqslant 0.100$, whereas samples with $x \leqslant 0.075$ have a cubic structure at room temperature. The structural phase transitions from $I4/mcm$ to $Pm\text{-}3m$ for the $0.020 \leqslant x \leqslant 0.150$ compositions were found to occur at higher temperature (T_C) on increasing x. For $x = 0.150$, T_C agrees with the temperature of permittivity anomaly reported by Durán *et al.* [6] and in all the cases the ϕ vs T dependence was consistent with a second-order transition as found in undoped $SrTiO_3$. All the doped samples exhibited active polar Raman modes consistent with the presence of PNRs at $T = 300$ K, independent of their long-range phase. Our local structure analysis revealed that also a local AFD distortion is active, even within a long-range cubic structure ($0.020 \leqslant x \leqslant 0.075$ at $T = 300$ K). Local tilting angle values agree with the theoretical predictions given in [11], helping to explain the coexistence of AFD and FE instabilities. Based on results presented here, we propose the structural phase diagram of $Sr_xPr_{1-x}TiO_3$ in the $0.020 \leqslant x \leqslant 0.150$ range and we argue that the cooperative model proposed by Aschauer and Spaldin [11] can reconcile the strongly competing FE and AFD states.

II. EXPERIMENTAL TECHNIQUES AND METHODS

$Sr_{1-x}Pr_xTiO_3$ samples with $x = 0$, 0.020, 0.035, 0.050, 0.063, 0.075, 0,100, 0.125, and 0.150 were prepared by standard solid-state reaction [4–7] using TiO_2 (Sigma-Aldrich 99.8%), $SrCO_3$ (Sigma-Aldrich 99.9%), and Pr_6O_{11} (Sigma-Aldrich 99.9%). Stoichiometric mixtures of as-received reagents were uniaxially pressed into disks and fired in Pt crucibles for 4 h at $T = 1400$ K, 4 h at $T = 1550$ K, and finally 4 h at $T = 1650$ K in static air atmosphere with intermediate regrindings until single-phase samples were obtained.

We performed temperature-dependent synchrotron x-ray powder diffraction experiments at the ID22 beamline of the European Synchrotron Radiation Facility (ESRF). High-resolution diffraction patterns of all the doped samples were collected between 90 and 650 K using incident photon beam with $\lambda = 0.319\,94$ Å. Data for pair distribution function (PDF) analysis were collected using a two-dimensional (2D) detector (PerkinElmer XRD 1611CP3) and $\lambda = 0.161\,02$ Å ($Q_{max} = 28$ Å^{-1}) for selected samples ($x = 0$, 0.020, 0.050, 0.075, 0.100, 0.125, and 0.150) at $T = 300$ K.

Rietveld analysis was performed through the GSAS program [13]. The background was subtracted using shifted Chebyshev polynomials and the diffraction peak profiles were fitted with a modified pseudo-Voigt function [13]. In the last refinement cycles all the parameters were refined: cell parameters, atomic positional degrees of freedom, isotropic thermal parameters, background, diffractometer zero point, and line profile parameters.

Selected diffraction powder patterns were reduced to the PDF using the formalism of the $G(r)$ function as implemented in the PDFGETX2 program [14]. $G(r)$ is obtained from the total structure factor $S(Q)$ via the sine Fourier transform (FT):

$$G(r) = \frac{2}{\pi}\int_{Q=0}^{Q_{max}} Q[S(Q) - 1]\sin(Qr)dQ, \qquad (1)$$

where $Q = 4\pi \sin\theta/\lambda$ and r is the interatomic distance. $S(Q)$ is the experimental coherent x-ray scattering intensity after correcting the raw data for sample self-absorption, for multiple scattering, and for Compton scattering.

Structure refinements against the $G(r)$ curves were carried out using the PDFGUI program [15]. The program assesses the accuracy of the refinement by the agreement factor (R_w) defined as follows [15]:

$$R_w = \left[\frac{\sum wi\left(G_i^{exp} - G_i^{calc}\right)^2}{\sum wi\left(G_i^{exp}\right)^2}\right]^{1/2}. \qquad (2)$$

Raman measurements were performed on a Renishaw RA 100 Raman analyzer at the Swiss-Norwegian Beam Lines (SNBL) at ESRF. Spectra were collected at $T = 300$ K on the samples with $x = 0$, 0.020, 0.050, 0.075, 0.100, 0.125, and 0.150 using a 532-nm (green) excitation wavelength at 2 mW in backscattering mode. Exposure time was 40 s for all the samples.

III. RESULTS AND DISCUSSION

At room temperature, the $0.020 \leqslant x \leqslant 0.075$ samples are isostructural to $SrTiO_3$ and the cubic $Pm\text{-}3m$ model gives a satisfactory description of our data. For $0.100 \leqslant x \leqslant 0.150$, instead, the split (200) reflection and the unperturbed (111) reflection family are rather consistent with a tetragonal cell with dimensions $\sqrt{2}a_p \times \sqrt{2}a_p \times 2a_p$, where a_p is the parent cubic cell parameter ($a_p \sim 3.90$ Å). The extra weak reflections detected in these patterns are, according to space group analysis [16,17], most compatible with the $I4/mcm$ space group. As to the temperature-dependent data, Fig. 1(a) shows for $x = 0.020$ portions of patterns around the (200) reflection at selected temperatures. At $T \sim 200$ K the $x = 0.020$ sample undergoes a structural phase transition signaled by the split (200) reflection and by the emergence of weak superlattice reflections [see Fig. 1(b)] as found for $x \geqslant 0.100$ at room temperature. The $I4/mcm$ model properly fits all the ensuing low-temperature patterns and, similarly, for every sample with $0.020 \leqslant x \leqslant 0.075$ we found the $Pm\text{-}3m$ to $I4/mcm$ phase transition on cooling. Vice versa, the room-temperature $I4/mcm$ phase of the samples with $x \geqslant 0.100$ evolves into the cubic $Pm\text{-}3m$ phase on heating to 400–500 K.

To facilitate comparisons between different phases, the tetragonal cell parameters (a_T, c_T) were reduced to the parent

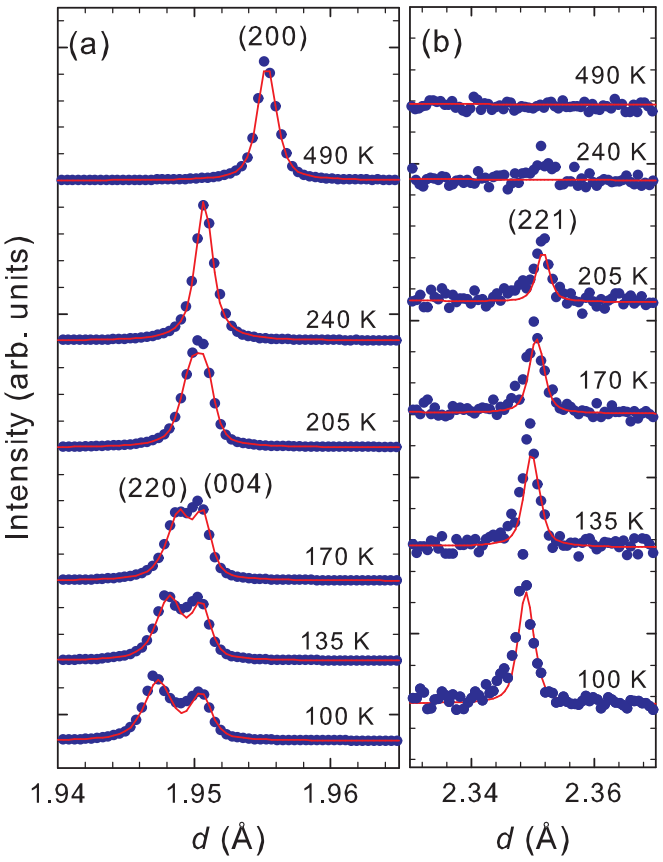

FIG. 1. Two selected ranges of the XRPD patterns of the $x = 0.020$ sample at different temperatures across the structural phase transition, showing in (a) the split of the (200) reflection into (220) and (004); in (b) the emergence of the (221) superstructure reflection. Dots are experimental data; continuous lines are the profiles calculated through Rietveld refinements; peaks are labeled with the respective Miller indexes. Rietveld agreement factors [$R(F^2)$] between observed and calculated patterns in the $Sr_{1-x}Pr_xTiO_3$ series ranged from 0.06 to 0.08.

cubic cell metric ($a_p = a_T/\sqrt{2}$; $c_p = c_T/2$) and plotted in Figs. 2(a)–2(c) as a function of temperature. For all the compositions, data show a temperature-independent behavior of c, as opposed to the Debye-like expansion in the direction of a. Their combined effect is a remarkable, x-dependent rise in tetragonality ($\eta = c_p/a_p - 1$) on cooling below the phase transition [Fig. 2(d)]. Increasing Pr concentration also causes a larger departure of the oxygen atom in the $8h$ site (O2) from its undistorted position in the perovskite structure ($xO2 = 0.25$), so that we could quantify the AFD order parameter by calculating the TiO_6 tilting angle (ϕ) from $xO2$ through $\tan(\phi) = 1-4(xO2)$. Plotted in Fig. 3, the amplitude of ϕ as a function of temperature is well fitted by a mean-field equation $\phi(T) = \phi(0)(1-T/T_c)^{\beta}$ (solid lines in Fig. 3), where $\beta \sim 0.5$ confirms the second-order character of the transition. Hence each $Sr_xPr_{1-x}TiO_3$ member features the same structural phase transition with a higher critical transition temperature (T_C) on increasing x (see Fig. 4) up to $x = 0.10$ with a small decrease of T_C values for $x = 0.125$ and $x = 0.15$. The observed composition dependences of ϕ and T_C indicate a progressive stabilization of AFD rotations at higher temperature following the decrease of the calculated tolerance factor (t) [8] (see Fig. 4), in agreement with previous neutron diffraction measurements [7].

The results of our Rietveld analysis are clearly not consistent with a long-range FE transition. First, in the canonical representation of the FE transition the structure evolves into a noncentrosymmetric phase, accommodating a continuous, macroscopic cation displacement that accounts for the emergence of dipole moments. The observation of dielectric permittivity maxima at $T_m = 500$ K in $Sr_xPr_{1-x}TiO_3$ [4] might suggest a PE (paraelectric) to FE transition on cooling below T_m. But T_m is almost doping independent and never matches our measured T_C; likewise the polarization hysteresis curves for $0.020 \leqslant x \leqslant 0.150$ are only slightly influenced by Pr concentration [4,6]. Second, the distortion parameters (ϕ,η) and the critical temperature (T_C) of the nonpolar AFD transition are amplified by increasing the dopant concentration, whereas a stronger AFD instability should suppress the polar FE mode, according to Zhong and Vanderbilt [8]. Third, the samples with $x \leqslant 0.075$ show no sign of long-range tetragonal distortion between T_C and T_m ($200 \leqslant T \leqslant 500$ K), despite the observed room-temperature FE in the whole $0.020 \leqslant x \leqslant 0.150$ range.

We tried to decouple the contribution of the long-range AFD distortion from that of FE by looking for a structural response across T_m in the cubic phase of $x \leqslant 0.075$ samples, in which the AFD mode is not active. As an example, we show in Fig. 5(a) the variation of the lattice parameter in the $x = 0.035$ case in a temperature range well into the cubic regime. On lowering the temperature from $T = 650$ K, the T evolution of the a parameter follows a Debye-like linear contraction. However, around a critical temperature, it shows an anomalous dilatation that denotes a linear trend on further cooling. This departure from the expected linear thermal contraction found for samples up to $x = 0.063$ can be attributed to electrostrictive strain [18–20]. For the $x = 0.020$, 0.035 samples, the corresponding critical Burns temperatures (T_B) are higher than the dielectric relaxation peak maximum at T_m, in agreement with previous observations [19].

Plotting all the T_B critical temperatures obtained in the T-x phase diagram of $Sr_xPr_{1-x}TiO_3$ (Fig. 4) evidences a distinct phase regime within the cubic region. We evaluated electrostrictive strain as $a_{observed} - a_{expected}/a_{expected} = QP^2$ [20]: $a_{observed}$ is the observed lattice parameter; $a_{expected}$ is the lattice parameter obtained by linear fitting the data points above T_B; P is the local polarization; Q is a constant factor. Thus the anomalous temperature evolution of the cubic lattice parameter below T_B translated into a steep rise of $Q' = \sqrt{QP^2}$ that looks qualitatively similar for all the samples [Fig. 5(b)].

Differently, the onsets of the electrostrictive strain at T_B were higher for $x = 0.020$ and $x = 0.035$ than for $x = 0.050$ and $x = 0.063$. On the one hand, for $x = 0.020$, 0.035 T_B is constant and also consistent with the x-independent T_m (see Fig. 4); as previously proposed [19], this is a possible scenario explaining the emergence of the dipole moment through the formation of local FE ordering. On the other hand, the decrease in T_B at $x = 0.050$ and $x = 0.063$, and so the absence of any electrostrictive effect at $x = 0.075$, strongly suggests a drop in spontaneous polarization as Pr concentration is increased

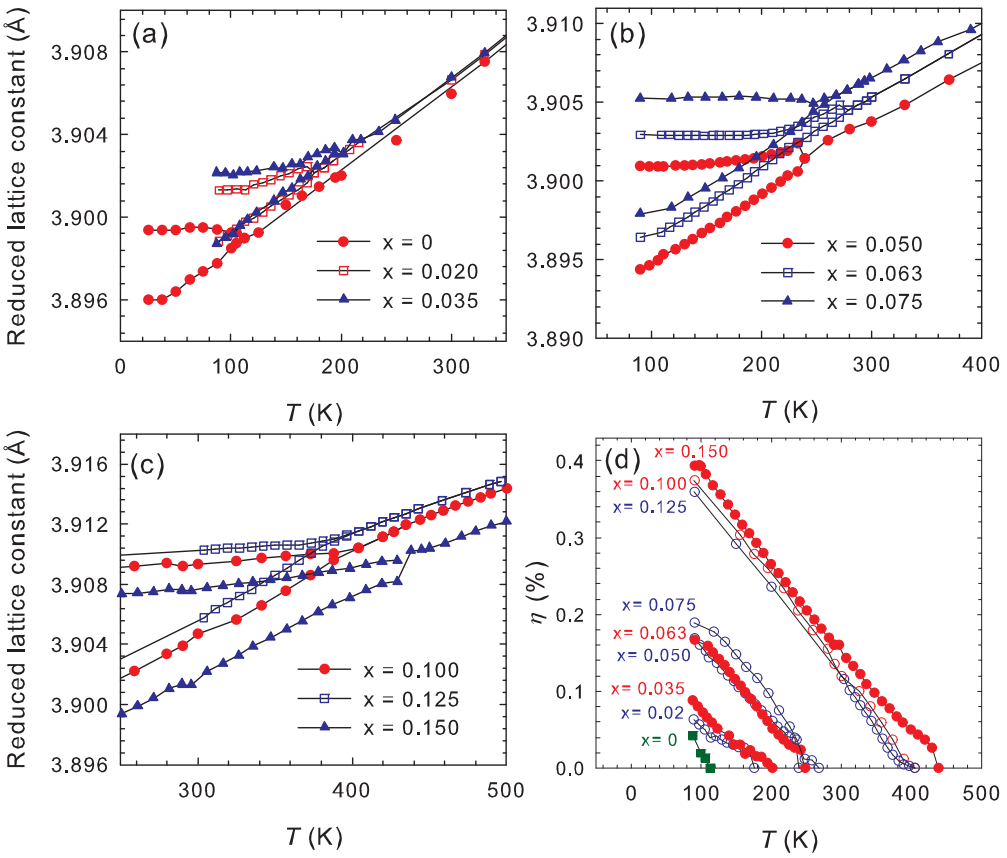

FIG. 2. (a–c) Temperature evolution of the cell parameters reduced to the cubic parent cell. The panels show subsequent groups of three compositions. Below the transition point at T_C the c axis is greater than the a axis. (d) Cell tetragonality expressed as $\eta = 1-c/a$ as a function of temperature for all the samples. Data for $x = 0$ below $T = 90$ K are taken from [33].

over $x = 0.035$. We could ascribe this polarization drop to the stronger AFD instability above $x = 0.075$ suppressing the FE mode [8], in this case, by inhibiting any local order that would give rise to electrostrictive strain. Thus, with no sign of electrostrictive strain in the high-x part of the phase diagram, a more exhaustive picture is needed to reconcile the $Sr_xPr_{1-x}TiO_3$ structure with the emergence of a FE state in the doped samples.

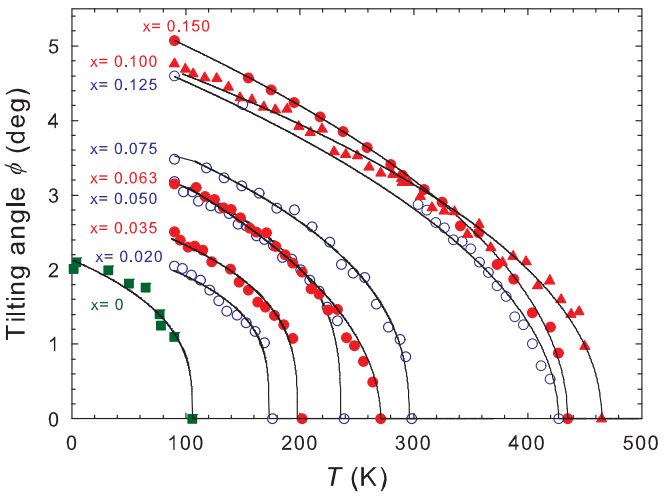

FIG. 3. Temperature evolution of the octahedral tilting angles (ϕ) obtained by Rietveld refinements for all the samples. Data for $x = 0$ are taken from [34]. The continuous lines are the best fits for the critical equation (see text).

We now turn our attention to the local structure of $Sr_xPr_{1-x}TiO_3$. We performed PDF-quality measurements on selected samples at $T = 300$ K to match the FE hysteresis measurements' temperature [4,6]. To keep our approach model independent, we fitted directly the PDF peaks corresponding to nearest-neighbor Ti-O and Sr/Pr-O distances with a parametrized Gaussian function to get the local interatomic distance values [PDF peaks labeled in Fig. 6(a)].

The Ti-O distances obtained by PDF and by Rietveld at $T = 300$ K, corresponding to the local and to the long-range atom-pair distances, respectively, are compared in Fig. 6(b). A clear divergence is visible already at $x = 0.020$: Opposite to the weak x dependence of the long-range Ti-O, the local Ti-O distance expands significantly on increasing x until it levels off for $x = 0.100$. In the $x = 0.150$ sample the local Ti-O distance is stretched by $\Delta \sim 0.015$ Å with respect to the long-range Ti-O distance, a mismatch the same order of magnitude as the Ti displacement in lead-based ferroelectrics [9,10].

The analysis of the Sr/Pr-O first shell evidenced an even more marked discrepancy between local and long-range structures. By comparing the short-range PDF of the $x = 0$ sample with that of the $x = 0.150$ sample [see Fig. 6(a)], one sees a sharp, single Gaussian peak for $x = 0$ but a

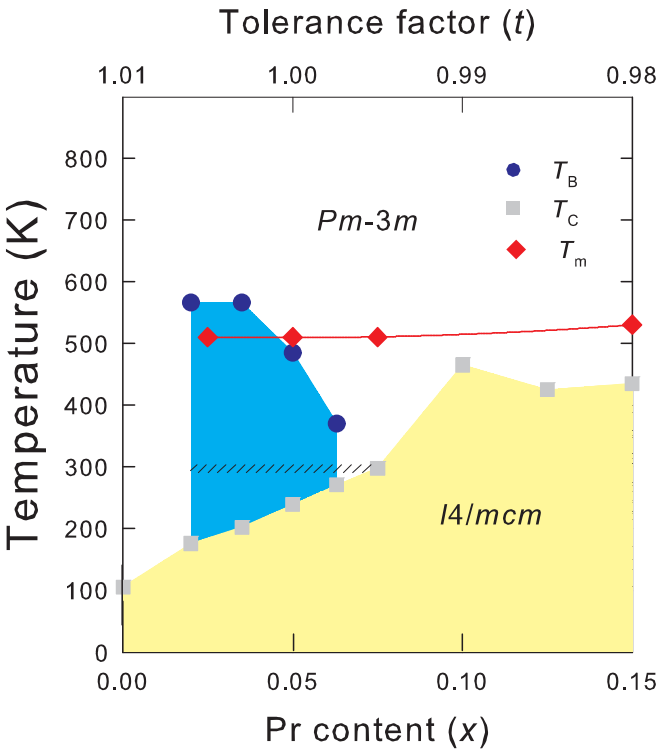

FIG. 4. Phase diagram proposed for $Sr_{1-x}Pr_xTiO_3$ in the $0 \leqslant x \leqslant 0.15$ range. For $x = 0$ the T_C is taken from [1]. The region delimited by the Burns temperature (T_B) is shaded in blue. Full squares denote the long-range structural phase transition and full diamonds indicate the onset of anomaly observed in dielectric constant measurements at T_m taken from [4,6]. A horizontal dashed line indicates the range where the mismatch between local and long-range structures is found. The secondary abscissa reports the perovskite tolerance factor (t) corresponding to x in the primary abscissa.

broad bond-length distribution for $x = 0.150$. This difference matches the respective long-range structures: Undistorted cubic $Sr_xPr_{1-x}TiO_3$ has a set of twelve identical Sr/Pr-O distances; by tilting the TiO_6 this set splits into three subshells containing four distances each, namely, Sr/Pr-O1 ($d \sim 2.76$ Å

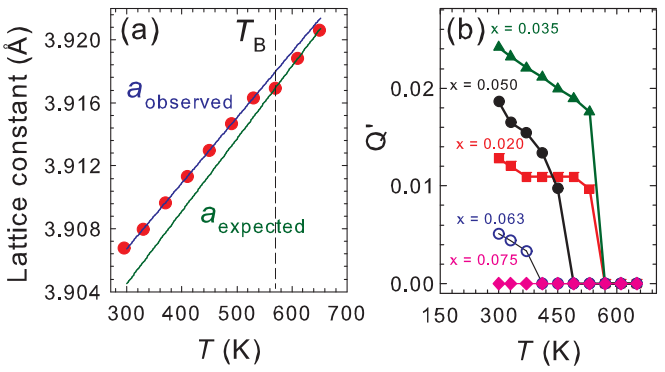

FIG. 5. (a) High-temperature evolution of the cubic lattice parameter a for $x = 0.035$ shown as an example (full circles). Straight lines show the temperature dependences of $a_{observed}$ and $a_{expected}$ (see text). (b) Temperature dependence of electrostrictive strain order parameter ($Q' = \sqrt{QP^2}$).

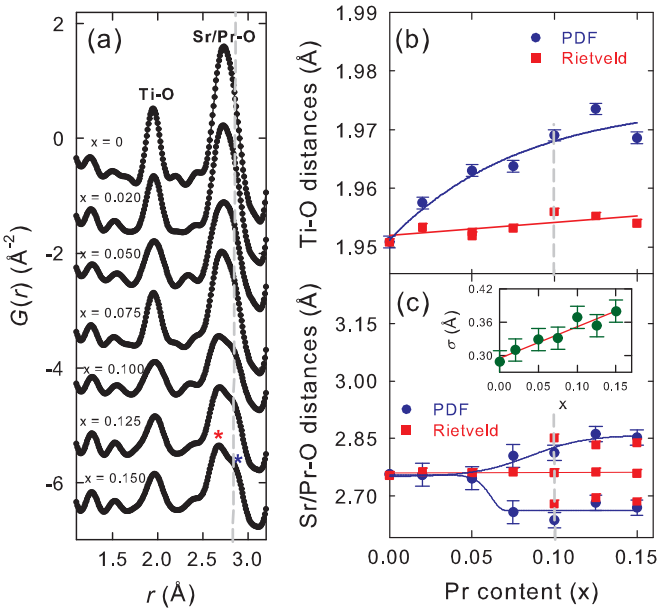

FIG. 6. (a) PDF peaks related to nearest-neighbor Ti-O and Sr/Pr-O at $T = 300$ K as a function of x. Patterns are offset for clarity. The vertical dashed line marks the position of high-r Sr/Pr-O subshell. (b) Ti-O distance values as a function of Pr content (x) at $T = 300$ K. (c) Sr/Pr-O distance values as a function of Pr content (x) at $T = 300$ K. The vertical dashed line indicates the x value above which the long-range cubic to tetragonal phase transition is observed at $T = 300$ K. Full squares are data obtained by Rietveld while full circles are values determined by fitting directly the PDF peaks. Inset to panel (c) shows the doping evolution of PDF Sr/Pr-O peak width (σ). For the sake of comparison, a single Gaussian function was used to evaluate σ at $x \geqslant 0.075$.

for $x = 0.150$), $Sr/Pr\text{-}O2_{short}$ ($d \sim 2.68$ Å for $x = 0.150$), and $Sr/Pr\text{-}O2_{long}$ ($d \sim 2.86$ Å for $x = 0.150$). As shown in Fig. 6(c), for $x = 0$ the local Sr-O distance matches the long-range Sr-O distance whereas for $x \geqslant 0.100$ the PDF resolution is not able to discriminate between Sr/Pr-O1 and the two sets of Sr/Pr-O2. As a result, the PDF signal consists of a doublet in which the low-r and high-r side centroids coincide with $Sr/Pr\text{-}O2_{short}$ and $Sr/Pr\text{-}O2_{long}$ obtained by Rietveld refinement. Unexpectedly, for $x = 0.075$ the PDF Sr/Pr-O peak is split into these two Sr/Pr-O tetragonal-like distances despite its long-range structure being well into the cubic region at $T = 300$ K (see Fig. 4). In addition, the mean width (σ) of the Sr/Pr-O bond-length distribution increases constantly with increasing x, as shown in the inset of Fig. 6(c). Since the σ parameter reflects the static and dynamic disorder of all the atom pairs involved, this provides a direct indication that the local/long-range structural mismatch involves a local symmetry lowering already at $x = 0.020$.

We tried to identify the structural model most consistent with the observed PDFs by carrying out profile refinements in the $1.6 \leqslant r \leqslant 12$ Å range. In agreement with previous neutron [21] and synchrotron [22] total scattering measurements, our observed PDF of undoped $SrTiO_3$ is well reproduced by the long-range cubic structure. For the $x \geqslant 0.100$ samples a tetragonal $I4/mcm$ model, as in the long-range structure, gave a very good agreement with the local PDF. For the samples with

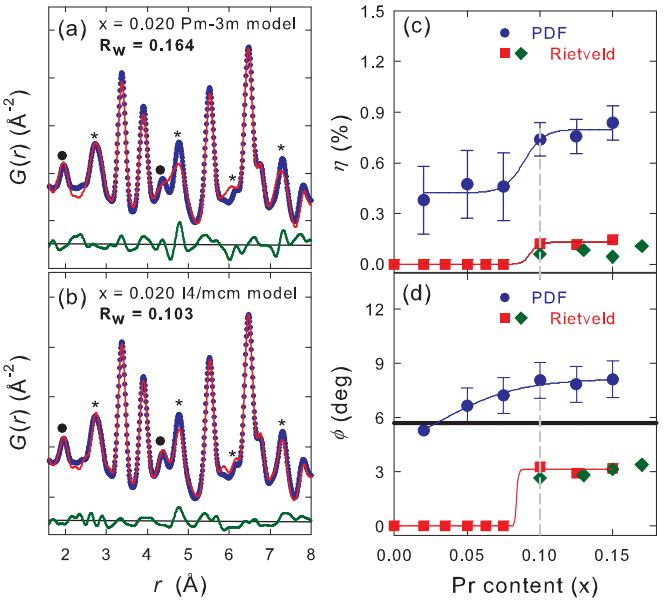

FIG. 7. (a,b) Short-range observed (dots) and calculated (continuous lines) PDF for $x = 0.020$ at $T = 300$ K obtained by fits using the cubic average model (a) and the tetragonal model (b). The symbols in both panels label the PDF peaks related to Ti-O (full circles), and Sr/Pr-O (stars), interatomic distances. (c,d) Values of tetragonality (η) and tilting angle (ϕ) as a function of Pr content (x). Full squares are data obtained by Rietveld refinements while full circles are the results obtained by PDF analysis on the local scale. The horizontal solid line marks the theoretical ϕ_{eq} value obtained in [11]. Experimental data taken from [7] are also reported in both panels for comparison (full diamonds).

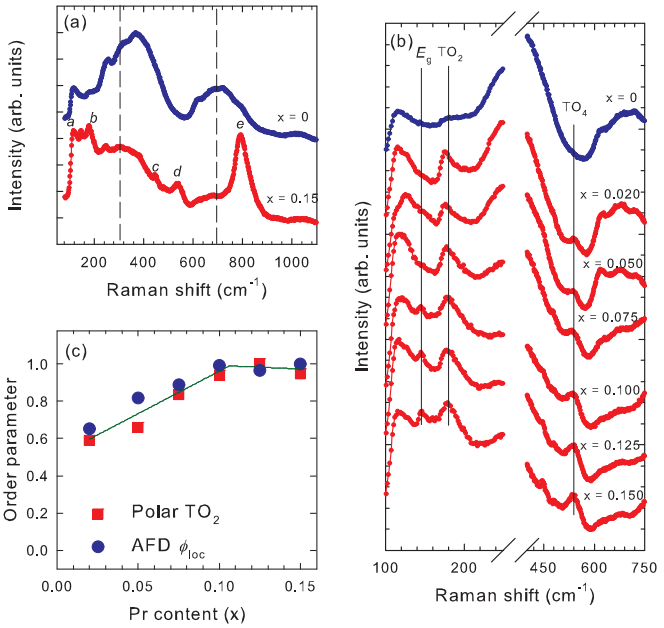

FIG. 8. (a) Room-temperature Raman spectra of undoped $SrTiO_3$ and doped ($x = 0.150$) samples. The modes identified and considered in the present work for discussion are labeled in alphabetical order in the $x = 0.150$ spectrum. (b) Selected regions of the Raman spectra at room temperature for $x = 0$, 0.020, 0.050, 0.075, 0.100, 0.125, and 0.150. Vertical dashed lines mark the principal identified E_g, TO_2, and TO_4 modes. (c) Doping evolution of normalized ϕ_{loc} as obtained from PDF (squares) and normalized integrated intensity of the TO_2 Raman mode (circles).

$x \leqslant 0.075$, however, a model based on the respective Pm-3m long-range structures was not as accurate: the PDFs calculated using this model underestimated the intensity of several experimental peaks. As shown, for example, in Figs. 7(a) and 7(b) for $x = 0.020$, a sensible improvement in fit quality was obtained by appyling the same $I4/mcm$ model we used for the highly doped samples ($x \geqslant 0.100$). In particular, the marked features in panel (a) are properly described only by fitting the lower-symmetry model.

It is worth noting that the local/long-range structural mismatch concerns only the short-range order. PDF fits performed in a range spanning to $r \geqslant 20$ Å were in fact insensitive to the choice of model, since the fits using either Pm-3m or $I4/mcm$ gave comparable agreement. It should be also pointed out that PDF fits using lower-symmetry models explicitly accounting for polar distortions were unfruitful. For example, by considering [001] or [110] as the polar directions and applying the appropriate cation displacements, the space group $I4/mcm$ produces the polar $I4cm$ and $Ima2$ subgroups, respectively [23]. When these polar models were tested against the PDF data, in spite of a significant increase in the number of refinable parameters, neither of them improved the fit quality in any case, and refinements were also unstable.

Having found that the $I4/mcm$ model consistently returned the closest PDF fits for all the compositions, we extracted the best-fit parameters in the $1.6 \leqslant r \leqslant 12$ Å range to quantitatively assess the structural discrepancy evidenced by peak fitting. Thus we obtained the values of local tetragonality (η_{loc}) and local tilting angle (ϕ_{loc}) shown in Figs. 7(c) and 7(d) and compared with the respective average values, obtained by Rietveld analysis. On the long-range scale both the ϕ and η order parameters are nonzero only for $x \geqslant 0.100$, as dictated by the structural phase transition and in close agreement with structural data reported by Garg *et al.* [7]. On the local scale, instead, both ϕ_{loc} and η_{loc} have nonzero values in all the doped samples ($x \geqslant 0.020$) and, in particular, both local parameters are greater than the respective values on the long-range scale anywhere in the tetragonal region of the phase diagram ($\phi_{loc} \geqslant 6°$, $\eta_{loc} \geqslant 0.4$).

To gain a better understanding of the compositional dependence of the AFD local structure we analyzed a series of Raman spectra measured at $T = 300$ K. The room-temperature spectrum of $SrTiO_3$ [see Fig. 8(a)] consists mainly of two second-order scattering broad bands centered at ~300 and ~700 cm^{-1}, both due to the overlapping of different combination modes belonging to cubic symmetry (m-3m) [5,24]. As Pr concentration is increased, the breakdown of cubic symmetry selection rules gives rise to distinct first-order modes, which gradually appear in the spectra of doped samples. The main modes are labeled in accordance with previous works [5,24], as shown in Fig. 8(a) for $x = 0.15$: (a) 145, (b) 175, (c) 445, (d) 540, and (e) 795 cm^{-1}. Two hard modes, at 145 and 445 cm^{-1}, were identified as E_g and B_{1g} [24] whereas the bands at 175, 540, and 795 cm^{-1} were attributed to the TO_2, TO_4, and LO_4 modes, respectively [5,24]. In the following

discussion we focus on the compositional dependence of the E_g, B_{1g} structural modes and of the TO_2, TO_4 polar modes.

Figure 8(b) reports the Raman spectra of $Sr_xPr_{1-x}TiO_3$ ($0 \leqslant x \leqslant 0.150$) in the Raman shift range of interest. Both the E_g and B_{1g} structural modes are clearly visible for $x \geqslant 0.100$ and, after careful inspection, weak modulations at 145 and 445 cm^{-1} are visible as well in $x = 0.075$. These two modes represent the effect of the rotation angle of TiO_6 around the c axis due to the freezing of the triply degenerate R_{25} phonon at the R point of the first Brillouin zone; thus their occurrence is expectedly limited to the sample within the tetragonal region of the phase diagram, or very close to it, as $x = 0.075$.

Turning our attention to the TO_2, TO_4 modes, the spectra in Fig. 8(b) show that bands related to both these hard polar modes are present in every sample except pure $SrTiO_3$. This provides evidence that even the lowest Pr concentrations induce PNRs, as already hinted at by spontaneous electrostrictive strain. The emergence of the TO_2 and TO_4 polar modes has been in fact related to the relaxational frequencies of PNRs in several Ti-based and Ta-based relaxors, for example, Ca-doped $SrTiO_3$ [24] and in Li- and Nb-doped $KTaO_3$ [25,26]. In particular, in ABO_3 perovskites, the low-frequency TO_2 mode is the so-called Last mode and represents the oscillation of A cations against BO_6 octahedra [27]. The higher-frequency TO_4 mode is the Axe mode, which corresponds to the bending of the oxygen cage in octahedra [27]. The presence of both these modes can be then considered the signature of polar instability [24–26]. In our case the x dependences of the frequency centroids of the polar modes are weak, but the intensity trends are quite revealing. In particular, the TO_2 intensity smoothly increases with x and then levels off when $x \geqslant 0.100$ [see Fig. 8(c)]. If the polar TO_2 intensity and the AFD ϕ_{loc} extracted from PDF fits are normalized to unity and plotted together, it becomes clear that the two parameters have the same dependence on composition [see Fig. 8(c)].

We assumed the TO_2 intensity as a gauge of the polar distortion associated with PNRs and ϕ_{loc} as its structural equivalent. According to available theory, for a spherical FE region embedded in a tetragonal host structure the TO_2 intensity reflects the autocorrelation function ($\langle P^2 \rangle$) of the spatially and temporally fluctuating, impurity-induced polarization $P(r,t)$ [22,28]. In the same way, the PDF stands for the autocorrelation function of the real space depending on the fluctuations from the average electron density given by local structural disorder, which is largely enhanced by doping. Thus the correlation between a purely FE order parameter and a purely AFD order parameter implies that local structural deviations quantified by the local AFD increase can actually originate from fluctuations in local dipole moment, expressed by PNRs.

We tried to figure out the interplay between local atomic fluctuations and the competitive instabilities in the average centrosymmetric structure and thus we propose the following simple picture. Doping with Pr affects the cubic structure of $SrTiO_3$ in two different ways. First, the smaller size of Pr^{3+} replacing Sr^{2+} decreases the perovskite tolerance factor, driving the nonpolar, AFD transition from $Pm\text{-}3m$ to $I4/mcm$ to much higher temperatures than $T_C = 105$ K (as in $SrTiO_3$). Second, the higher charge of Pr^{3+} replacing Sr^{2+} should generate positively charged point defects ($Pr^{\bullet}_{Sr}$) which must be compensated by negatively charged defects such as Sr and Ti vacancies (V''_{Sr}, V''''_{Ti}) and/or Ti'_{Ti} [29]. The Coulombic attraction of these oppositely charged defects has been considered a likely driving force for cation off-centering, giving rise to dielectric dipoles around which PNRs can form [29]. The retention of inversion symmetry through the cubic-tetragonal transition accompanied by an increasing AFD character in the long-range phase agrees with early first-principles calculations predicting that a strong AFD distortion practically suppresses the FE mode [8]. Moreover, within the PDF resolution, we found the centrosymmetric, AFD $I4/mcm$ model the one most consistent with the local structure of every sample at $T = 300$ K, even when concomitant with the long-range cubic phase. The absence of a polar structural order seems to conflict with the observation of dielectric permittivity peaks [4–7] and of polar Raman modes (see above).

On the other hand, the coexistence of these conflicting phenomena can be explained by considering the combined effect of tetragonality and tilting angle, which largely characterizes the local structure of $Sr_xPr_{1-x}TiO_3$, and which Aschauer and Spaldin recently studied [11]. In particular, they found a theoretical equilibrium angle ($\phi_{eq} = 5.7^\circ$) below which the suppression of FE by the AFD instability is energetically favorable: Because of charge transfer between Ti-O σ^* and Sr-O σ^* bonds, which decreases the antibonding orbital overlap, the Ti-O bonds are strengthened, ultimately suppressing Ti off-centering. However, above ϕ_{eq} the increased tetragonality associated with the AFD instability makes the structural distortion energetically favorable towards recovering the loss of Ti-O π bonding along the c axis; this allows the polar instability to rise beyond the amplitude normally computed for the cubic perovskite.

Our experimental results match this scenario. All ϕ_{loc} values are above ϕ_{eq} in the whole $0.020 \leqslant x \leqslant 0.150$ range [Fig. 7(d)] and each sample shows increased tetragonality; e.g., for $x = 0.150$, η_{loc} is about four times larger than any η value found on the long-range scale. The appearance of TO_2 and TO_4 polar modes accounts for PNRs formation in all the doped samples and the correlation between the TO_2 intensity and the ϕ_{loc} reinforces the evidence that AFD and FE instabilities are intimately entangled in $Sr_xPr_{1-x}TiO_3$. Based on these results, we argue that AFD and FE instabilities do not only coexist, but they are also compatible with a centrosymmetric long-range structure because of the local cooperative effect of η_{loc} and the persistence of PNRs induced by doping.

The structural findings reported here clarify some peculiar properties of $Sr_xPr_{1-x}TiO_3$. The reported relaxor FE behavior at T_m can be fully related to the freezing of the PNRs detected by Raman, which coexists with local highly tilted and tetragonally distorted regions observed by PDF. The slight dependence of T_m on the Pr concentration must not be compared to the second-order phase transition, from which T_m is decoupled, but rather to the weak compositional dependence of the ϕ_{loc} and η_{loc}. In addition, we mention a recent report on low lattice thermal conductivity at high temperature [30] that designated $Sr_xPr_{1-x}TiO_3$ as new thermoelectric materials with a high figure of merit. This implies an additional phonon scattering mechanism for the carriers that would follow the magnitude fluctuations of TiO_6 tilt described here.

As a final point, we would like to note that, with respect to other doped $SrTiO_3$ systems [23,31,32], Pr induces a markedly different structural effect. The first difference concerns the symmetry breaking: Whereas all Ba, Pb [23], or Sn [31] drive the symmetry reduction from $Pm\text{-}3m$ towards polar space groups, Pr-doped $SrTiO_3$ mantains the soft-mode phase transition of the undoped material. The second difference deals with the relationship between long-range and local structure. Cubic samples of $Sr_{1-x}Pr_xTiO_3$ have lower local symmetry, and the AFD instability is greatly enhanced in tetragonal samples. By contrast, the AFD local structure of $SrTi_{1-x}Nb_xO_3$ is remarkably similar to the long-range phase [32] whereas $Sr_{1-x}Sn_xTiO_3$ is dominated by the stereochemical lone-pair effect and undergoes a local symmetry decrease only at low temperature [31]. These features make $Sr_{1-x}Pr_xTiO_3$ more akin to the undoped compound than to other doped $SrTiO_3$.

IV. CONCLUSION

We presented structural results on $Sr_xPr_{1-x}TiO_3$, a perovskite known to show relaxor ferroelectricity at room temperature. For $0.020 \leqslant x \leqslant 0.150$ we studied the AFD $Pm\text{-}3m$ to $I4/mcm$ structural phase transition, which occurs at a higher temperature on increasing x. In agreement with a reduced tolerance factor, a higher Pr concentration boosts the structural distortion parameters related to the AFD instability. Conversely, all the samples feature TO_2 and TO_4 hard polar Raman modes, which are consistent with the presence of PNRs.

As generally reported in the literature, coexisting FE and AFD instabilities tend to be in strong competition and to cancel out. On the other hand, our local structure analysis evidenced local AFD distortions much larger than in the long-range AFD structure, independent of Pr concentration and even within a long-range cubic phase. The locally enhanced tilting angles were in quantitative agreement with recent theoretical calculations on $SrTiO_3$ [11], supporting the idea that a strong local AFD mode promotes, rather than disrupts, the polar instability, even in the absence of long-range cation displacements. This provides a mechanism accounting for the polar instability in relaxor FE perovskite oxides.

ACKNOWLEDGMENTS

We thank the ESRF for provision of beam time on ID22 and C. Drathen for her kind assistance during experiments CH-4024 and CH-4324. We also thank W.Van Beek and D. Chernyshov for assisting in the Raman measurements at the SNBL.

[1] K. A. Müller and H. Burkard, Phys. Rev. B **19**, 3593 (1979).
[2] R. E. Cohen, Nature **358**, 136 (1992).
[3] G. A. Samare, J. Phys.: Condens. Matter **15**, R367 (2003).
[4] A. Durán, E. Martinez, J. A. Diaz, and J. M. Siqueiros, J. Appl. Phys. **97**, 104109 (2005).
[5] R. Ranjan, R. Hackl, A. Chandra, E. Schmidbauer, D. Trots, and H. Boysen, Phys. Rev. B **76**, 224109 (2007).
[6] A. Durán, F. Morales, J. Fuentes, and J. M. Siqueiros, J. Phys.: Condens. Matter **20**, 085219 (2008).
[7] R. Garg, A. Senyshyn, H. Boysen, and R. Ranjan, Phys. Rev. B **79**, 144122 (2009).
[8] W. Zhong and D. Vanderbilt, Phys. Rev. Lett. **74**, 2587 (1995).
[9] Chen Ang, Zhi Yu, J. Hemberger, P. Lunkenheimer, and A. Loidl, Phys. Rev. B **59**, 6665 (1999).
[10] V. Lemanov, Phys. Solid State **39**, 1468 (1997).
[11] U. Aschauer and N. A. Spaldin, J. Phys.: Condens. Matter **26**, 122203 (2014).
[12] J. H. Haeni, P. Irvin, W. Chang, R. Uecker, P. Reiche, Y. L. Li, S. Choudhury, W. Tian, M. E. Hawley, B. Craigo, A. K. Tagantsev, X. Q. Pan, S. K. Streiffer, L. Q. Chen, S. W. Kirchoefer, J. Levy, and D. G. Schlom, Nature **430**, 758 (2004).
[13] A. C. Larson and R. B. Von Dreele, Los Alamos National Laboratory Report No. LAUR 86-748 (2004).
[14] X. Qiu, J. W. Thompson, and S. J. L. Billinge, J. Appl. Crystallogr. **37**, 678 (2004).
[15] C. L. Farrow, P. Juhas, J. W. Liu, D. Bryndin, E. S. Bozin, J. Bloch, T. Proffen, and S. J. L. Billinge, J. Phys.: Condens. Matter **19**, 335219 (2007).
[16] M. Allieta, M. Scavini, L. J. Spalek, V. Scagnoli, H. C. Walker, C. Panagopoulos, S. S. Saxena, T. Katsufuji, and C. Mazzoli, Phys. Rev. B **85**, 184107 (2012).
[17] P. M. Woodward, Acta Crystallogr., Sect. B **53**, 32 (1997).
[18] G. Burns and F. H. Dacol, Phys. Rev. B **28**, 2527 (1983).
[19] R. Ranjan, R. Garg, R. Hackl, A. Senyshyn, E. Schmidbauer, D. Trots, and H. Boysen, Phys. Rev. B **78**, 092102 (2008).
[20] L. E. Cross, Ferroelectrics **76**, 241 (1987).
[21] C. J. Howard and H. T. Stokes, Acta Crystallogr., Sect. A **61**, 93 (2005).
[22] Q. Hui, M. G. Tucker, M. T. Dove, S. A. Wells and D. A. Keen, J. Phys.: Condens. Matter **17**, S111 (2005).
[23] Y. Yoneda and S. Kohara, Ferroelectrics **485**, 34 (2015).
[24] U. Bianchi, W. Kleemann, and J. G. Bednorz, J. Phys.: Condens. Matter **6**, 1229 (1994).
[25] J. Toulouse, P. DiAntonio, B. E. Vugmeister, X. M. Wang, and L. A. Knauss, Phys. Rev. Lett. **68**, 232 (1992).
[26] P. DiAntonio, B. E. Vugmeister, J. Toulouse, and L. A. Boatner, Phys. Rev. B **47**, 5629 (1993).
[27] V. Goian, S. Kamba, J. Hlinka, P. Vaněk, A. A. Belik, T. Kolodiazhnyi, and J. Petzelt, Eur. Phys. J. B **71**, 429 (2009).
[28] U. Bianchi, J. Dec, W. Kleemann, and J. G. Bednorz, Phys. Rev. B **51**, 8737 (1995).
[29] I. A. Sluchinskaya, I. A. Lebedev, and A. Erko, J. Appl. Phys. **112**, 024103 (2012).
[30] A. M. Dehkordi, S. Bhattacharya, J. He, H. N. T. Alshareef, and M. Terry, Appl. Phys. Lett. **104**, 193902 (2014).
[31] G. Laurita, K. Page, S. Suzuki, and R. Seshadri, Phys. Rev. B **92**, 214109 (2015).
[32] K. Page, T. Kolodiazhnyi, T. Proffen, A. K. Cheetham, and R. Seshadri, Phys. Rev. Lett. **101**, 205502 (2008).
[33] A. Okazaki and M. Kawaminami, Mater. Res. Bull. **8**, 545 (1973).
[34] J. M. Kiat and T. Roisnel, J. Phys.: Condens. Matter **8**, 3471 (1996).